Journal of Materials Chemistry A

ROYAL SOCIETY OF CHEMISTRY

PAPER

View Article Online
View Journal | View Issue

Cite this: J. Mater. Chem. A, 2025, 13, 32590

Enhanced air stability by calcium doping in $Na_{2/3}[Fe_{1/2}Mn_{1/2}]O_2$ cathode material for Na-ion batteries

Monalisha Mahapatra, Zachary T. Gossage, Changhee Lee, Shinichi Kumakura, Kodai Moriya and Shinichi Komaba *

Surface instability under ambient conditions in layered sodium transition metal oxides, such as P2 type $Na_{2/3}[Fe_{1/2}Mn_{1/2}]O_2$ (NFM), leads to initial capacity loss, poor cyclability, and gelation of the polyvinylidene fluoride slurry through defluorination. Although NFM is a high-performance cathode material, primarily due to its high capacity and stable electrochemical behavior, this issue presents a significant challenge to its practical application in low-cost sodium ion batteries. In this study, we investigated Ca^{2+} doping into the Na^+ layer of NFM to enhance structural and environmental stability. We found that Ca^{2+} doping at 1 wt.% improved crystallinity and increased interlayer spacing which led to an improved rate performance while maintaining high discharge capacities of 190 mAh g^{-1}. Furthermore, the air and water stability of the Ca^{2+}-doped NFM samples was significantly improved, as demonstrated *via* X-ray diffraction, transmission electron microscopy, and other analyses. While the as-synthesized undoped samples exhibited a rapid Na^+/H^+ exchange process, we found that this reaction was suppressed in Ca-doped samples. Electrochemical testing after 2 days of air exposure showed that NFM lost ~35% of its discharge capacity, but Ca-doped samples showed no losses. Based on surface analyses, the improved stability appears to stem from spontaneous Ca migration during air exposure which leads to a Ca-enriched surface layer that suppresses decomposition processes such as Na^+/H^+ exchange and Na deintercalation. This previously undescribed mechanism appears to be quite effective in mitigating surface degradation reactions in layered oxides.

Received 11th June 2025
Accepted 12th August 2025

DOI: 10.1039/d5ta04742k

rsc.li/materials-a

1. Introduction

Sodium-ion batteries (SIBs) have drawn considerable interest as a cost-effective and sustainable alternative to lithium-ion batteries, particularly for large scale energy storage.[1] SIBs utilize naturally abundant electrolyte and electrode components, while showing similar intercalation chemistry to lithium.[2] Currently, research efforts are heavily focused on improving electrode materials for attaining high performance SIBs including major strides in carbon materials for the negative electrode[3,4] and high-performance positive electrode materials based on layered transition metal oxides (Na_xTmO_2, $x = 0$–1, Tm = transition metal).[5,6] Na_xTmO_2 oxides are some of the most promising positive electrode materials for SIBs due to their simple synthesis and structural versatility,[7] but they can show several limitations including structural degradation and irreversible phase change during cycling, poor air/moisture stability and limited energy densities depending on the material structure and cutoff voltage.[8,9] Improving the positive electrode remains a major goal for attaining practical and high performance SIBs.

Following Delmas' nomenclature, Na_xTmO_2 usually crystallizes into two structures, P2 and O3, differentiated by their Na^+-coordination environment with oxygen (P: prismatic; or O: octahedral) and the stacking sequence of the $(MO_2)_n$ slabs.[10] While both types are actively being researched, P2 type materials with Na^+ occupying a prismatic site tend to show faster Na^+ diffusion and better cyclability compared with O3.[11] Our group previously reported P2 $Na_{2/3}[Fe_{1/2}Mn_{1/2}]O_2$ (NFM) which delivered a high reversible capacity (190 mAh g^{-1}) and energy density (520 mWh g^{-1}) in sodium cells using only earth-abundant elements.[12] While the usage of Fe and Mn is highly desirable for next-generation energy storage,[13] NFM and other materials incorporating these transition metals are known to degrade under ambient conditions showing hygroscopicity, Na^+/H^+ exchange and generation of surface impurities (*e.g.* hydroxides and carbonates).[8,14] This exchange process can negatively impact charge/discharge performance and the slurry making process.[8] Also, P2 materials are susceptible to the insertion of water and CO_2 due to their Na deficiency and increased interlayer distances.[15,16] The intercalation of H_2O expands the interlayer distance of the Na^+ layers forming hydrated oxide

Department of Applied Chemistry, Tokyo University of Science, Shinjuku, Tokyo 162-8601, Japan. E-mail: komaba@rs.tus.ac.jp

phases.[17] This issue presents a major hurdle for commercialization as materials with poor air stability lead to higher production costs and require strict control of transport, storage and processing environments.[18] Therefore, there is significant interest in enhancing the intrinsic stability of NFM and other layered oxides.

In recent years, researchers have been exploring various methods to improve the stability of layered oxides including surface coatings and elemental doping. Surface coatings, such as Al_2O_3[19] and MgO[20] and other phosphate-based surface layers coatings[21] have been reported as a plausible strategy to enhance material stability. However, surface coatings do not alter the inherent material properties, making them susceptible to defects or pinholes and requiring fine tuning of other parameters (*e.g.* surface coating thickness, adhesion, *etc.*). On the other hand, we can take advantage of the extensive synthetic diversity of layered oxides and partially substitute other transition metals or elements for Na, Fe or Mn during the synthesis process. Thus, doping is well-known to strongly impact the structure and performance of various battery materials. For layered oxides, some reports have shown that substitution of Cu,[22] Ni,[17] and Li[23] into the TM layer can help suppress water insertion and improve air stability. Also, Zhao *et al.* showed that Nb^{5+}-doping could induce the formation of a surface preconstructed layer in P2 $Na_{0.67}Mn_{0.67}Ni_{0.33}O_2$.[24] Although these results are promising, most of the materials studied so far show relatively low capacities of ~100 mAh g^{-1} or less and few studies have focused on high capacity materials like NFM. With these previous reports in mind, there seems to be significant promise in doping the NFM structure to overcome air stability issues while maintaining high reversible capacities.

In addition to previously mentioned dopants, Ca is an excellent choice as a dopant due to its non-toxic nature and abundance as one of the most common elements on Earth.[8,25,26] Ca doping has already been reported to suppress Na^+/H^+ exchange and improve air stability in other layered oxides.[27,28] Also, to the best of our knowledge, researchers of Sumitomo Chemical Co., Ltd first found and reported that Ca doping is efficient in reducing the hygroscopic character of O3 $Na[Fe_{0.4}Ni_{0.3}Mn_{0.3}]O_2$.[8,26] Aside from its impact on air stability, Tao *et al.* confirmed that Ca^{2+} doping stabilizes the O3-type structure and increases the interlayer spacing which can improve the rate performance.[29] However, Ca doping has not been explored for improving air stability and electrode performance in NFM or other layered oxides consisting predominantly of Fe–Mn. Herein, we focus on doping Ca^{2+} at low concentrations to improve the air stability of NFM, *e.g.* $Na_{0.65}Ca_{0.01}[Fe_{0.5}Mn_{0.5}]O_2$. We found that introducing Ca^{2+} into the Na^+ layer had minimal effect on the charge/discharge performance and capacity but showed major improvements in air stability. No losses in discharge capacity were observed after 2 days of storage at 65% relative humidity (RH). Based on scanning transmission electron microscopy (STEM) analysis, we could identify a Ca-enriched surface layer that formed while the particles were exposed to air. We speculate that this surface layer is key to maintaining the layered structure and preventing decomposition in air. Furthermore, the rate performance of the Ca-doped materials was significantly improved compared to undoped NFM, indicating Ca doping as a promising strategy for enhancing the stability and performance of NFM.

2. Experimental methods

2.1 Material synthesis

Ca-doped NFM, $Na_{2/3-2x}Ca_xFe_{1/2}Mn_{1/2}O_2$ ($x = 0$, 0.01, 0.02), in which charge neutrality is considered for the partial substitution of Ca^{2+} for Na^+, was synthesized using solid state reaction methods with stoichiometric amounts of the starting materials: calcium hydroxide ($Ca(OH)_2$), iron oxide (Fe_2O_3), manganese oxide (Mn_2O_3, prepared from $MnCO_3$, Aldrich, by heating under air at 900 °C for 12 h) and 5 wt% excess of sodium carbonate (Na_2CO_3, Nacalai Tesque, 99.8%). The starting materials were thoroughly mixed through ball milling with acetone at 300 rpm for 12 h. After ball milling, the milled powder samples were dried, pelletized and calcined at 900 °C for 12 h and then quenched by quickly transferring into an Ar-filled glovebox.[30] For hygroscopic tests, the powdered samples were further exposed to 65% relative humidity in air for 5 days or were also immersed in distilled water for 7 days and then filtered.

2.2 Material characterization

Phase purity and crystal structures of $Na_{2/3-2x}Ca_xFe_{1/2}Mn_{1/2}O_2$ were examined using X-ray diffraction (XRD, Multiflex, Rigaku Co.,Ltd) equipped with a high-speed, one-dimensional X-ray detector. Non-monochromatized Cu Kα radiation was utilized as the X-ray source with a nickel filter. During data collection, the samples were protected from air exposure using a sealed laboratory-made holder. XRD results were used for generating a schematic illustration of the crystal structure using the program VESTA. Synchrotron XRD patterns were collected at beam line BL02B2, SPring-8 in Japan, equipped with a large Debye–Scherrer camera.[31] The wavelength of the incident X-ray beam was set to 0.5 Å using a silicon monochromator, which was calibrated with a CeO_2 standard. Structural analysis by the Rietveld method was carried out using the powder profile refinement program, General Structure Analysis System (GSAS-II).[32] Particle morphologies and elemental content were further analysed with scanning electron microscopy (SEM, JCM-6000, JEOL Ltd) equipped with an energy dispersive X-ray spectrometer. X-ray absorption spectroscopy (XAS) was conducted at beamline BL-7C of the photon factory at KEK Japan. XAS spectra were collected with a silicon monochromator in transmission mode. The intensity of the incident and transmitted X-rays was measured at room temperature. High resolution (HR)-TEM and STEM analyses of pristine and air exposed samples were conducted using a JEOL JEM-2100F equipped with a JEOL JED-2300T at the National Institute of Materials Science (NIMS).

2.3 Surface characterization

Na^+ exchange and surface stability of the synthesized materials was evaluated using pH measurements in an immersion test. After dispersing the powder in deionized water, the samples were immersed in water, left for varying times while stirring, and then removed by filtration and the filtrate pH was

subsequently measured. X-ray photoelectron spectroscopy (XPS) was performed (PHI 5000 VersaProbe II) with micro-focused scanning X-ray source Al Kα (1486.6 eV) radiation at NIMS and the deconvolution of the XPS spectra was performed with Origin software. The binding energy of each XPS signal was adjusted based on the C 1s (sp^2 C–C) peak at 284.5 eV. The intensities were further normalized based on the Fe 2p (Fe $2p_{3/2}$) peak intensity for semi-quantitative analysis. Attenuated Total Reflectance Fourier-Transform Infrared (ATR-FTIR) spectroscopy was performed on both doped and undoped samples before and after air exposure. Reference spectra of bare Na_2CO_3 and $CaCO_3$ powders were also acquired under identical conditions for comparison.

2.4 Electrochemical characterization

For charge–discharge testing, the working electrodes were prepared inside an Ar-filled glove box. The slurry consisted of a mixture of 80 wt% active material, 10 wt% acetylene black (AB, stream Chemicals, Inc.) and 10 wt% poly(vinylidene fluoride) (PVdF, Polyscience, Inc.) dispersed in *N*-methyl-2-pyrrolidone (Kanto Chemical Co., Ltd). After thoroughly mixing the slurry by hand with a mortar and pestle, the slurry was coated on aluminium foil and dried at 100 °C under vacuum. Electrochemical tests were carried out with a R2032 type coin cell using the prepared working electrodes, Na metal counter electrodes, and a glass fibre separator (BG-100R, ADVANTEC, Co). The electrolyte consisted of 1.0 mol dm^{-3} (M) $NaPF_6$ dissolved in propylene carbonate (PC) (Kishida Chemicals Co). All charge–discharge tests were conducted in the voltage range of 1.5–4.3 V (*vs.* Na) at a rate of C/20 (1C = 259 mA g^{-1}) in a thermostatic chamber at 25 °C.

3. Results and discussion

We started by evaluating how Ca-doping incorporates into the P2 structure and impacts the stability of NFM. We synthesized P2 type layered oxides with the general formula $Na_{2/3-2x}Ca_x[Fe_{1/2}Mn_{1/2}]O_2$ (x = 0, 0.01, 0.02) *via* a conventional solid state reaction method at 900 °C. The structural properties of the synthesized materials were examined by XRD as shown in Fig. 1a. The undoped and 1% Ca doped NFMs exhibited a pure hexagonal P2 type structure with $P6_3/mmc$ symmetry.[33] From XRD, we observed improved crystallinity of the Ca-substituted sample with sharper XRD peaks and a reduced full width half maximum (FWHM) at $2\theta = 38.3°$ (Fig. S1). Despite no detectable secondary Ca-containing phases, we confirmed the uniform

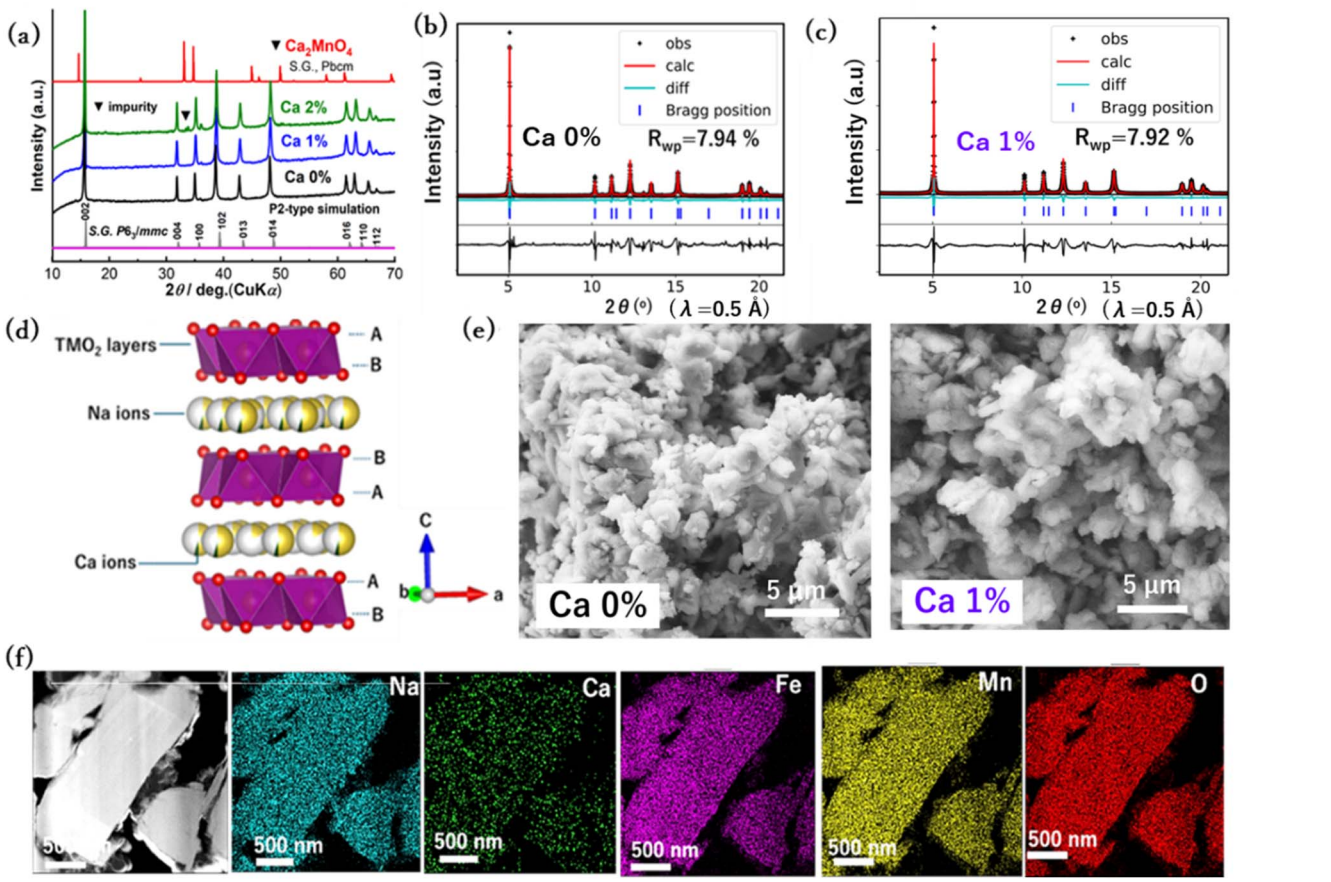

Fig. 1 (a) XRD patterns of P2–$Na_{2/3-2x}Ca_x[Fe_{1/2}Mn_{1/2}]O_2$. Rietveld refinement of synchrotron XRD for (b) NFM and (c) NCFM. (d) Illustration of the corresponding crystal structure for the Ca-substituted sample. (e) SEM images of NFM and NCFM and (f) STEM-EDS mapping of the NCFM sample.

incorporation of Ca into the material *via* SEM-EDX (Fig. S2). No visible superstructure reflections were observed in the synchrotron XRD data, particularly in the $2\theta = 5$–$10°$ region, where superstructure peaks are typically observed for some layered oxides (Fig. S3).[34] Increasing the Ca-substitution to $x = 0.02$ in $Na_{2/3-2x}Ca_x[Fe_{1/2}Mn_{1/2}]O_2$ (Fig. 1a) retained the layered structure but also led to the formation of a minor impurity phase indexed to Ca_2MnO_4.[35] We believe that this may be indicative of a solubility limit for Ca^{2+} within the P2 framework.[25] To avoid complications from this impure phase, all further experiments were conducted on only NFM and the 1% Ca doping (NCFM) samples.

Further structural analysis was conducted using synchrotron XRD and Rietveld refinement on the NFM and NCFM samples. As summarised in Tables S1 and S2, the refined lattice parameters showed a slight increase in the *c*-axis from 11.215 Å for NFM to 11.227 Å for NCFM. Also, we directly observed interlayer expansion using HR-TEM (Fig. S4). Previously, Ca^{2+} doping has been reported to expand the Na^+ layer in other layered oxides, which is thought to result from the increased Na^+ vacancies with Ca^{2+} substitution.[36] At the same time, the *a*-axis exhibited only a slight contraction,[37] which suggests that Ca^{2+} expands the interlayer spacing without significantly disrupting the in-plane transition metal framework. The ionic radius of Ca^{2+} (~1.00 Å) is close to that of Na^+ (~1.02 Å), so it is reasonably expected that Ca^{2+} will substitute into the sodium layer instead of replacing Fe^{3+}(~0.64 Å) or Mn^{4+}(0.53 Å),[36] as supported by the Rietveld refinement (Table S2). Thus, a schematic illustration of the Ca-doped structure is provided in Fig. 1d.

The morphology of the Ca doped samples was analysed using SEM, which revealed spherical secondary particles with diameters ranging from 2 to 10 μm (Fig. 1e), with the undoped material exhibiting a smaller average particle size. We also evaluated the elemental distribution across the particles using STEM-EDS mapping as shown in Fig. 1f, which confirmed that Ca is uniformly distributed throughout the bulk of the particles. Likewise, Fe and Mn were evenly distributed throughout the doped (Fig. 1f) and undoped materials (Fig. S5). X-ray absorption near edge structure (XANES) analysis further indicated that the oxidation states of Fe and Mn were unaffected by Ca-doping (Fig. S6). In summary, Ca doping into the P2 type layered oxide NFM was successfully achieved with minimal effect on the crystal structure aside from the slight increase in interlayer spacing.

Following the structural analysis, we prepared composite electrodes from each material and evaluated the electrochemical performance and topotactic extraction/insertion of Na^+ ions from/into the layered oxides. As shown in Fig. 2a, the initial charge–discharge profiles of undoped and Ca 1%-doped materials showed similar profiles with discharge capacities of ~190 mAh g^{-1}. Despite Ca^{2+} occupying the Na^+ site, the small amount of Ca doping does not appear to negatively affect the sodium storage capabilities. From the differential capacity (d*Q*/d*V*) curves of the 2nd charge/discharge cycle in Fig. 2b, both samples exhibit clear and similar redox peaks corresponding to Na^+ insertion and extraction. The dominant redox features in the 2.0–2.5 V and 3.0–4.2 V ranges are mainly attributed to the Mn^{3+}/Mn^{4+} redox and Fe^{3+}/Fe^{4+} couples, respectively.[12] Notably the NCFM sample exhibits sharper and more intense redox

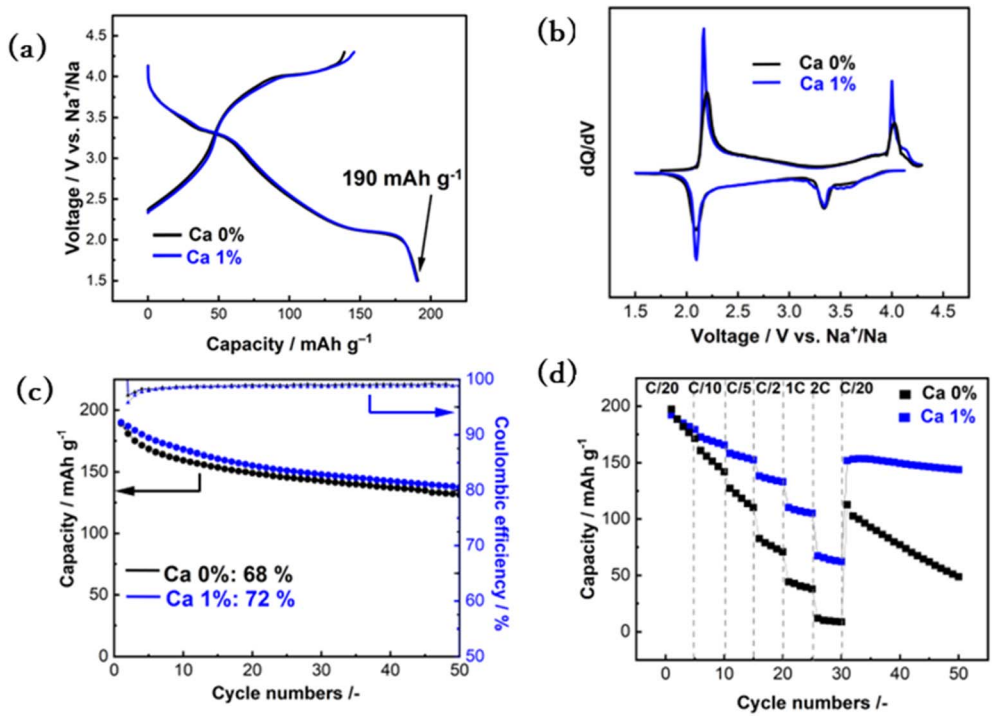

Fig. 2 (a) First charge–discharge profile of NFM and NCFM electrodes at C/20. (b) Differential capacity (d*Q*/d*V*) plots extracted from the second cycle. (c) Cycling performance during 50 cycles and (d) C-rate performance.

peaks compared to NFM, which suggests that Ca doping enhances the redox kinetics in agreement with previous reports.[27] During further cycling (Fig. 2c), the NCFM sample demonstrated slightly improved capacity retention of 72% compared to 68% for the NFM sample (Fig. S7). XRD analysis of the electrodes after 50 cycles (Fig. S8) confirmed that all the diffraction lines of the P2 phase were maintained in both NFM and NCFM electrodes. There was only a slight shift of the 002 peak to lower angles, which is linked to the sodium content in the material. It should also be taken into consideration that Ca^{2+} ions in the Na layer are electrochemically inactive and not readily extracted during cycling.[36] This can be attributed to the higher charge and strong electrostatic interaction of Ca^{2+} with the surrounding oxygen framework compared to Na^{+}. Additionally, the large charge density (z/r) of Ca^{2+} likely leads to deeper stabilization, making its extraction energetically unfavorable.

Next, we investigated the impact of Ca-doping on the rate performance of NFM. Again using coin cells, we increased the discharge rate from C/20 up to 2C (assuming a reversible capacity at 1C = 259 mAh g^{-1}) changing the rate every 5 cycles while the charging rate was maintained at C/20. We observed that Ca-doping significantly improved the discharge rate performance as shown in Fig. 2d and S8. At a high rate of 1C, the NFM electrodes showed low reversible capacities of only 44 mAh g^{-1}, while NCFM could deliver capacities of 110 mAh g^{-1}. Even at 2C, the Ca-doped electrodes maintain appreciable capacities (67 mAh g^{-1}) (Fig. S9) compared to the undoped sample (11 mAh g^{-1}). Since the particle size became large by the Ca doping, it seems that Ca doping can stabilize the layered structure and preserve the Na^{+} diffusion path within the particle.[29,35] Furthermore this improvement can also be understood from the perspective of ionic potential modulation as the higher ionic potential of Ca^{2+} in the Na layer may also reduce Na^{+}–Na^{+} repulsion within the interlayer space and smoothen the diffusion energy landscape, thereby indirectly facilitating Na^{+} migration.[38] Likewise, our results indicated both improved rate performance and interlayer expansion with Ca-doping, suggesting that small amounts of Ca doping (*e.g.* 1 mol%) can significantly enhance the electrochemical performance of NFM without any notable drawbacks. These enhancements can be attributed to the pillar effect of Ca^{2+} ions between the TmO_2 slabs, which act as a structural support for maintaining interlayer spacing, preventing structural collapse, and facilitating sustained Na^{+} diffusion during cycling.[39]

As mentioned in previous reports,[25,26,40] Ca doping has been shown to enhance the bulk structural stability of P2 type materials by suppressing degradation when exposed to ambient air. Building on this understanding, we investigated whether Ca doping could improve surface stability and prevent Na^{+}/H^{+} exchange at the particle surface. As illustrated in Fig. 3a, the synthesized powders were soaked in water for varying times with stirring. During soaking, Na^{+} leaching and H^{+} insertion in the NFM material should lead to an increase in pH according to the following equation.[8,41]

$$x\ H_2O + Na_{0.67}TmO_2 \rightarrow Na_{0.67-x}H_xTmO_2 + x NaOH \quad (1)$$

After soaking for a set amount of time, the NFM and NCFM particles were removed using filtration and the pH of the resulting filtrate solutions was measured (Fig. 3b). We noted a rapid pH increase for the NFM sample where the measured pH was ~11.4 after only 5 minutes of soaking. On the other hand, the pH for the NCFM sample only increased to ~9.1 over the same time period. This indicates that Na^{+}/H^{+} exchange at the NCFM material was significantly suppressed compared to NFM. For filtrate solutions after longer soaking, the pH gradually increased for both NFM and NCFM, which indicates continuous Na^{+} leaching and hydroxide buildup with time. Nevertheless, the suppression of Na^{+} leaching by Ca doping was consistent over time and NCFM was more stable.

Next, we evaluated whether Ca incorporation could enhance the material's resistance to atmospheric degradation, *i.e.* air exposure. In this case, the doped and undoped materials were exposed to air with ~65% relative humidity for several days, and their structural evolution was tracked by XRD. As shown in Fig. 4a, after 2 days of exposure the undoped NFM sample exhibited hydrated phases which consist of structural changes in the layered oxide caused by intercalation of water molecules into the interlayer spacing, leading to expansion and partial disruption of the original layered framework. This is further

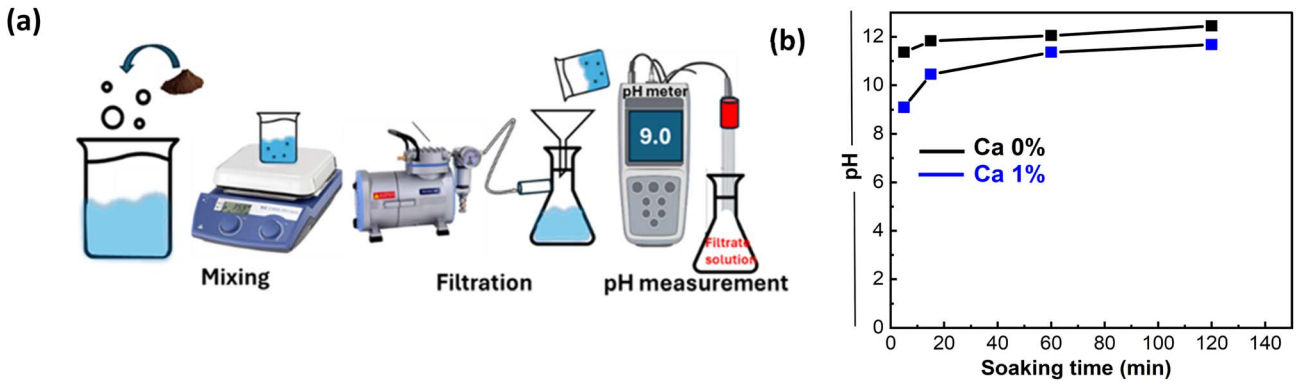

Fig. 3 (a) Scheme of the pH analysis method and (b) pH measurements of the filtrate solution after immersion of NFM and NCFM powders in DI water for various time intervals.

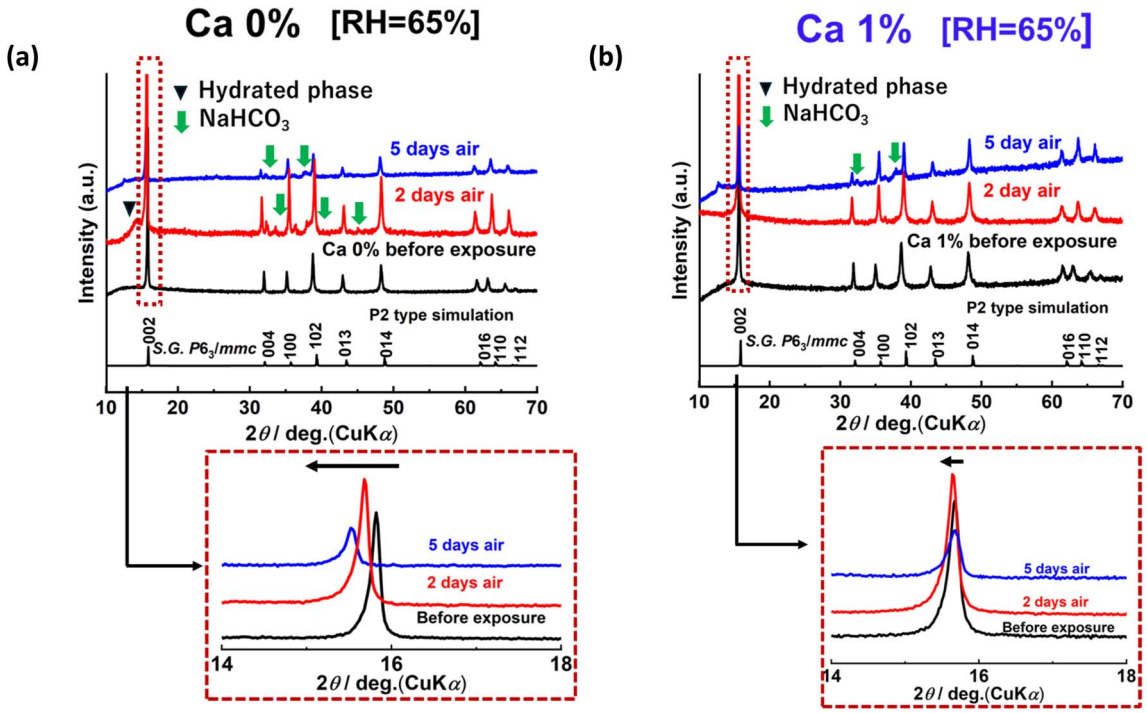

Fig. 4 X-ray diffraction (XRD) patterns of (a) NFM and (b) NCFM samples after exposure to air (RH 65%) for 0, 2, and 5 days.

supported by synchrotron XRD analysis, where the c-lattice parameters of the undoped sample increased from 11.215 Å (before 2 days of air exposure) to 11.244 Å (after 2 days of air exposure) (Fig. S10). The term "hydrated phase" is used by analogy with birnessite-type MnO_2, exhibiting a significant increase in interlayer spacing upon insertion of water molecules.[17] The XRD patterns also shows an impurity peak, including the formation of sodium bicarbonate, $NaHCO_3$, which can form by reaction of extracted Na^+ with atmospheric CO_2 and H_2O upon exposure, as follows:[17]

$$xCO_2 + H_2O + Na_{2/3}Fe_{1/2}Mn_{1/2}O_2 \rightarrow Na_{2/3-x}H_xFe_{1/2}Mn_{1/2}O_2 + xNaHCO_3 \quad (2)$$

Furthermore, the 002 diffraction peak, which is highly sensitive to interlayer spacing and sodium content,[17,42] showed significant shifting toward lower 2θ in XRD patterns of the undoped sample (Fig. 4, inset). In contrast, the 1% Ca doped sample demonstrated markedly improved air stability with no hydrated or $NaHCO_3$ peaks, and minimal shifting of the 002 peak after 2 days of air exposure (Fig. 4b). As observed in the pH measurements, Ca^{2+} incorporation into the sodium layer appears to suppress Na^+ migration and surface reactivity, which is likely due to the formation of strong Ca–O bonds and interlayer stabilization.[43] If we consider an analogous Ca-phase, *i.e.* $Ca_{1/3}$[Fe, Mn]O_2, we can expect it to show a higher redox potential for calcium extraction compared to that of sodium extraction from $Na_{2/3}$[Fe,Mn]O_2. When sodium is extracted from NFM and NCFM not only *via* electrochemical oxidation but also *via* Na^+/H^+ exchange and air oxidation,[8] calcium should not be easily extracted but be simply mobile, and finally enriched at the surface of NCFM particles. This may resist reactions with air and Ca^{2+}/H^+ ion exchange which leads to increased instability in NFM. If the calcium enriched surface of NCFM particles is formed and acts as a protective layer, perhaps the Na^+/H^+ exchange and reactions with moisture and CO_2 can be minimized, thereby enhancing both bulk and surface integrity and chemical stability. Extended exposure of the undoped sample for 5 days led to a decline in the peak intensities indicating a progressive loss in crystallinity and structural degradation. After longer exposure times, however, even the 1 mol% calcium substitution at the Na site in NCFM began to exhibit minor impurities and reduced crystallinity. Nevertheless, the calcium doped sample showed less peak shifting and broadening indicating higher stability as compared to the Ca-free sample.

Based on our understanding of the air exposure results, we assessed how air exposure affects electrode fabrication and electrochemical performance. We checked the influence on electrode slurry preparation in air (outside the glovebox) under ambient conditions using the PVdF binder and NMP solvent (Fig. S11). Notably, the NFM slurry exhibited severe gelation, leading to poor slurry uniformity and hindered electrode casting due to defluorination of PVdF.[8] In spite of partial gelation by the NCFM sample we can cast and coat the slurry on Al foil with acceptable homogeneity. For charge–discharge testing, composite electrodes were also prepared inside a glovebox from the undoped and Ca-doped samples after 2 days of air exposure (RH 65%). As shown in Fig. 5a, the air exposed NFM electrode exhibited a noticeable drop in discharge capacity by ~62 mAh g^{-1} without an increase in polarization. During further cycling (Fig. 5b), the NFM electrode showed poor capacity retention of

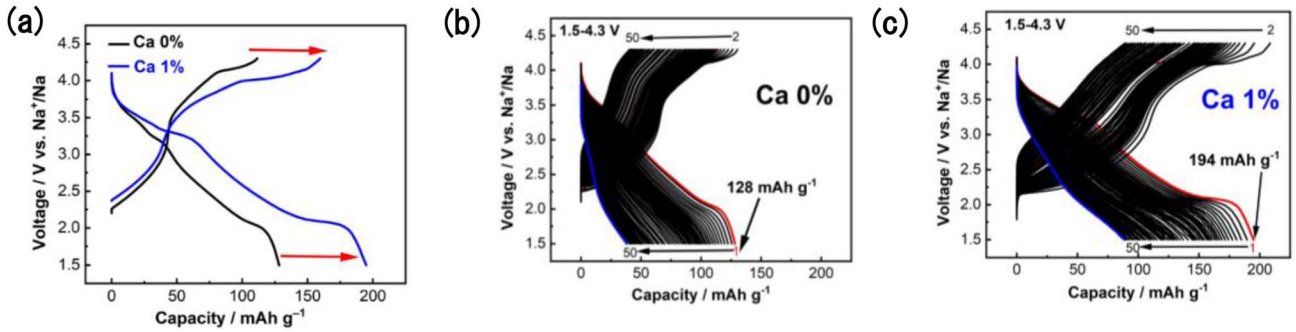

Fig. 5 (a) 1st charge–discharge of Ca-doped electrodes after 2 days of air exposure (RH 65%). Charge–discharge curves during further cycling for (b) NFM and (c) NCFM. All cycling was conducted at a C/20 rate.

31% after 50 cycles. In contrast, NCFM electrodes maintained high initial discharge capacities of ~190 mAh g^{-1} after air exposure (Fig. 5c) and improved cycling performance compared to the undoped sample after air exposure. In other words, no significant negative impact on reversible capacity and capacity retention was found for air-exposed and unexposed NCFM electrodes as shown in Fig. 2 and 5. These results suggest that Ca doping strengthens the surface protection, further maintaining the electrochemical integrity of the NCFM material for electrode processing and cyclability.

To further understand the origin of the improved surface stability in the Ca doped samples, we utilized STEM-EDS measurement on the NCFM sample before and after 2 days of air exposure (Fig. 6a). It was observed that Ca is more prominent at the surface after air exposure (further images provided in Fig. S12), which was not observed in the as-synthesized NCFM sample (see STEM-EDS data in Fig. 1f). When plotting the atomic percentage *vs.* distance (Fig. 6b), we observed no enrichment of Ca^{2+} or Na^{+} at the particle surface in the unexposed NCFM sample. However, after 2 days of air exposure, the Ca^{2+} dopant located at the sodium site of the P2 structure was enriched in the surface layer in the 0.3–0.4 μm region of the plots in Fig. 6c, implying that Ca^{2+} ions are thermodynamically driven towards the particles surface during air exposure. Because divalent cations like Ca^{2+} generally show much lower mobility in the oxide framework than monovalent Na^{+} due to stronger coulombic interaction of Ca^{2+}–O^{2-} bonds than Na^{+}–O^{2-} bonds, we think that Ca^{2+} ions tend to remain in the surface layer without oxidative extraction or Ca^{2+}/H^{+} ion exchange routes.

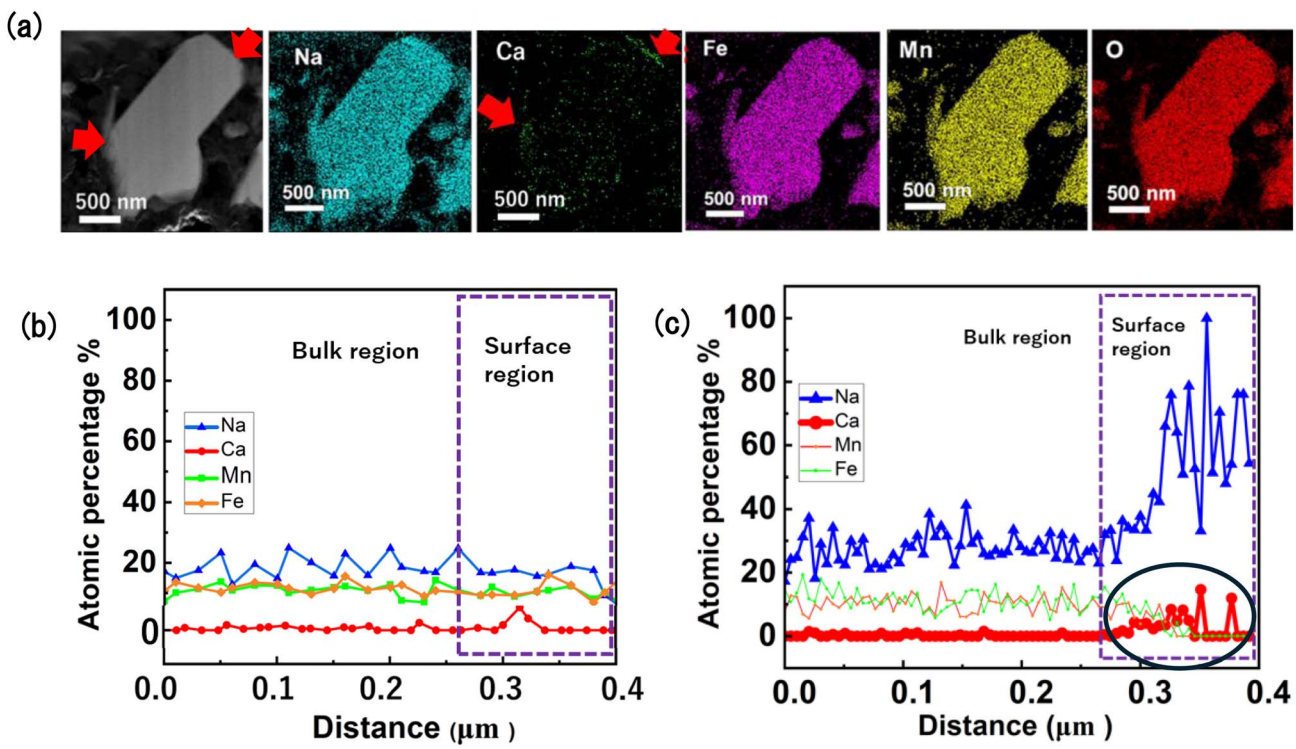

Fig. 6 (a) High resolution TEM image of the 1% Ca sample after 2 days of air exposure (RH 65%). The EDX line profile showing atomic percentage *vs.* distance for the Ca 1% particle (b) before and (c) after air exposure.

Furthermore, TEM/EDX shows that calcium is not uniformly distributed across the entire surface, but mainly enriched at the particle's edges, which are more reactive and prone to environmental degradation. These edge planes are critical for Na^+ transport and often act as an entry point for moisture and CO_2.[44] This spontaneous formation of a Ca-rich layer suggests that calcium ions migrate to the sites where reactions with air and/or moisture occur and protection is most needed. The layer is likely very thin, and the distribution may not be completely resolved by TEM/EDX. Additionally, rather than rapid structural degradation as seen in the undoped sample, the migration of Ca^{2+} to the surface appears to facilitate the formation of a Ca^{2+}- enriched or mixed Ca^{2+}–Na^+ phase that helps to protect the surface from further Na^+/H^+ exchange as described above. At the same time, TEM-EDX mapping suggests that distributions of Fe, Mn and O are not significantly impacted by air exposure and remain evenly distributed throughout the particles. Additionally, since the ionic radii of Ca^{2+} and Na^+ are almost identical, the Na^+ diffusion at the Ca-enriched surface would not be deteriorated because of the minimal modification of the P2-framework structure. However, it is worth noting that if surface accumulation of Ca becomes excessive – particularly under extended air exposure – it could lead to increased interfacial resistance and negatively affect the rate capability of the material. Such localized build up may hinder Na^+ transport especially at high current densities. While the results of our present study indicate that the Ca-enriched surface layer remains thin and beneficial under tested conditions, the long-term evolution of this layer and it impact on high-rate electrochemical performance require further investigation.

To further verify the Ca enriched surface layer, we used X-ray photoelectronic spectroscopy (XPS) before and after air exposure (Fig. 7). The XPS intensities were normalized based on Fe to provide semi-quantitative analysis of the Ca content. In both cases, the spectra show the presence of Ca–O bonding environments, suggesting that bulk 1% Ca doping is sufficient to observe an XPS signal or surface species such as CaO or $CaCO_3$ are formed during synthesis and storage. Notably, after air exposure, a clear shift in the Ca $2p_{3/2}$ peak from 346.0 eV to 346.5 eV was observed, indicating a change in the local chemical environment of calcium, possibly due to increased oxidation or carbonate formation. The peak width remained nearly the same, supporting that the shift is not due to broadening but rather a genuine chemical change. Additionally, after air exposure a noticeable increase in both the peak intensity and peak area of the Ca 2p signal were observed (Table S3), further confirming the TEM results. When considering the mechanism, we note that initially Ca^{2+} is uniformly doped in the bulk of the P2 NFM lattice, but air exposure particularly in humid environments appears to initiate the typical surface degradation processes through sodium loss and structural instability. The degradation may further create a chemical potential gradient and electrostatic imbalance near the surface, causing Ca^{2+} ions to slowly migrate outward. Once at the surface, we speculate that Ca^{2+} may (1) locally enrich and interact with the surrounding transition metal–oxygen framework. This may lead to a virtual Ca phase, resembling $Ca_{1/3}[Fe, Mn]O_2$, which could show a high redox potential and resist Ca^{2+}/H^+ ion exchange. Alternatively, the enrichment process may (2) involve the subsequent growth of a $CaO/CaCO_3$ rich or a similar passivation layer. For our further clarification ATR-FTIR spectroscopy was performed (Fig. S13) on all samples before and after air exposure, alongside reference measurements using pure Na_2CO_3 and $CaCO_3$. We could clearly observe carbonate at the air-exposed surface based on 1430 cm^{-1} and 875 cm^{-1} peaks but the resulting spectra could not clearly distinguish between calcium and sodium carbonate related peaks. In addition Ca compounds are known to be significantly more chemically robust and less prone to dissolution compared to Na^+ species like NaOH, Na_2CO_3, *etc.* Regardless of the surface species rich in Ca, there appears to be some progressive mechanism that is effective at blocking the Na^+/H^+ exchange pathway and preserving the bulk composition during air exposure.

In addition, to confirm our hypothesis we performed synchrotron XRD (SXRD) measurements followed by Rietveld refinement on the air exposed samples for both NFM and NCFM (Fig. S10). Although the fit quality is limited by slight peak broadening and possible minor changes in the surface but the results do not show any evidence of cation or anion vacancy formation in the bulk structure after air exposure. The only noticeable change is a slight decrease in the c-lattice parameters,

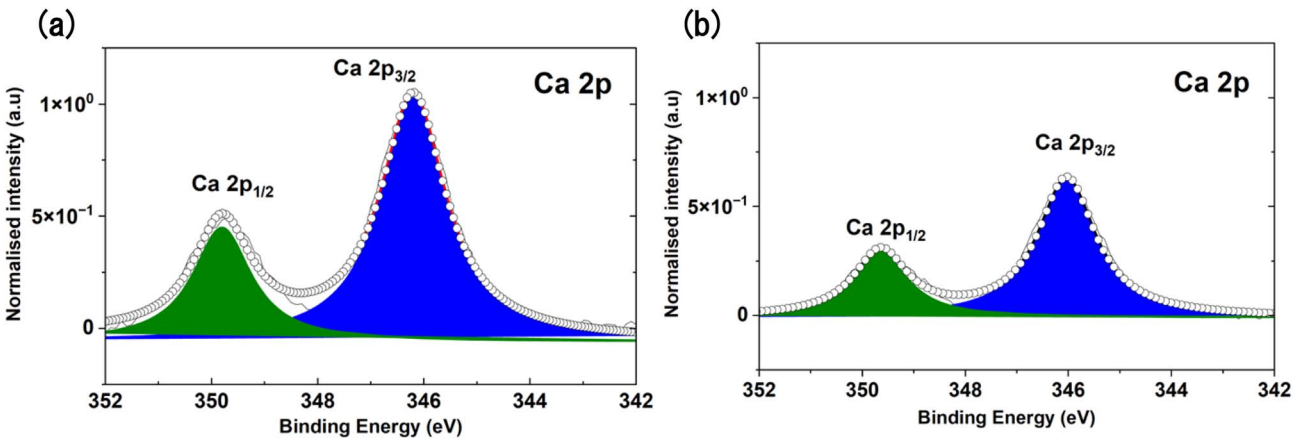

Fig. 7 XPS for Ca 2p region of NCFM (a) after air exposure (b) before air exposure.

from 11.227 Å (before air exposure) to 11.220 Å (after air exposure). For reference, the c-lattice parameter of undoped NFM was 11.215 Å. This shift places the post-air-exposed Ca-doped NCFM between the values of undoped and pre-exposure Ca-doped NFM. This suggests that air exposure induces minor structural relaxation, but not a complete reversion to the undoped phase.

As a final test, we chose to investigate the stability of NCFM in aqueous conditions, which is relevant for application of high-performance aqueous binders.[45,46] Both NFM and NCFM samples were subjected to water exposure for 15 minutes (similar to the time required for the slurry making process) and XRD spectra were collected. As shown in Fig. S14, NFM showed rapid decomposition with a large shift in the 002 peak after only 15 minutes of water exposure. On the other hand, the Ca-doped sample showed much higher stability with minimal shifting in the 002 peak. Even in this more extreme environment, Ca^{2+} seems to play a protective role in reducing the extent of Na^+ loss and suppressing structural decomposition. However, after 24 hours and 7 days of exposure, both samples exhibited new reflections in XRD corresponding to hydrated sodium carbonate ($Na_2CO_3.H_2O$) suggesting some decomposition.[14] We further evaluated the impact of water exposure (15 minutes) on the electrochemical performance (Fig. S15). Both samples showed a decline in their discharge capacity to 160 mAh g^{-1} and 142 mAh g^{-1} for the doped and undoped electrodes, respectively. As observed in the air exposure test, NCFM delivered comparatively better cycling stability compared with the undoped sample. Although the long term cyclability was not high for either sample, the results suggest that Ca incorporation mitigates the extent of performance degradation by partially suppressing surface reactions and stabilizing the electrode–electrolyte interface through a similar mechanism to that observed during air exposure testing.

4. Conclusions

In this work, we demonstrated the impact of doping Ca^{2+} into NFM as a strategy to improve its air and moisture tolerance. We find that Ca^{2+} can be readily doped into the Na interlayer with only a slight expansion of the interlayer distance and with minimal disruption of the transition metal layers. The charge/discharge profile and gravimetric capacities were unaffected by such low percentage doping (*e.g.* 1 wt%), but at the same time, doping improved the crystallinity and rate performance. Furthermore, through a combination of structural, chemical and electrochemical analyses, we firmly established that Ca incorporation greatly enhances the air and moisture stability of NFM. Air exposure seems to induce the formation of a surface enriched Ca layer, which likely acts as a protective barrier against continuous Na^+/H^+ exchange and carbonate formation. Even in high stress environments such as direct immersion into water, the Ca-doped NFM could maintain better capacity and cyclability. Overall, our findings suggest that Ca doping is a simple and promising way to modify the surface stability of layered oxides to facilitate more robust electrode processing, while at the same time having a minimal effect on the charge/discharge mechanism and attainable capacities.

While much progress is still required to overcome the various issues of NFM and other layered oxides for long-term battery performance, air stability can be significantly improved by atomic doping with low-cost elements such as Ca. We believe that *in situ* formation of surface-protecting layers as observed in this work is an interesting approach for future materials. We can expect that excessive surface accumulation of Ca could hinder Na^+ diffusion kinetics if not properly controlled, but this same limitation should also occur for pre-coating strategies. Unlike pre-coatings, the spontaneous formation of the protective interface observed in this work can progressively develop as needed. In addition, a co-doping strategy combining Ca with other elements like Cu and Ti[47] may further increase the air stability and performance, while still enabling Ca migration and protection. Based on the promising outcomes observed for $Na_{2/3}Fe_{0.5}Mn_{0.5}O_2$, we are currently extending this doping strategy to other layered oxides with different transition metal compositions (such as Fe–Ni, Mn rich, and Fe–Co systems) encompassing not only P2 type but also other O3/P3-type layered oxides to evaluate the generalizability of Ca-induced surface stabilization. As high performance materials like NFM are stabilized under ambient and aqueous conditions using Ca or other dopants, we anticipate the possibility of utilizing aqueous binder systems which offer numerous benefits compared to PVdF.[48]

Conflicts of interest

There is no conflicts to declare.

Data availability

Additional electrochemical performace, cycling data, HRTEM-EDS and EXSITU-XAS, ATR-FTIR results, detailed structural information are included in the SI. See DOI: **https://doi.org/10.1039/d5ta04742k**.

Acknowledgements

This study was partially funded by the Ministry of Education, Culture, Sports, Science and Technology (MEXT) Program: Data Creation and Utilization Type Materials Research. (JPMXP1122712807), the JST through CREST (Grant No. JPMJCR21O6), ASPIRE (JPMJAP2313), GteX (JPMJGX23S4), and JSPS KAKENHI Grant Numbers JP25H00905, JP24H00042, and JP20H02849. M.M. personally appreciates the Japan International Cooperation Agency (JICA-IITH FRIENDSHIP Scholarship 2.0).

References

1 K. Kubota, M. Dahbi, T. Hosaka, S. Kumakura and S. Komaba, *Chem. Rec.*, 2018, **18**, 459–479.
2 N. Yabuuchi, K. Kubota, M. Dahbi and S. Komaba, *Chem. Rev.*, 2014, **114**, 11636–11682.
3 Z. T. Gossage, D. Igarashi, Y. Fujii, M. Kawaguchi, R. Tatara, K. Nakamoto and S. Komaba, *Chem. Sci.*, 2024, **15**, 18272–18294.

4 D. Igarashi, Y. Tanaka, K. Kubota, R. Tatara, H. Maejima, T. Hosaka and S. Komaba, *Adv. Energy Mater.*, 2023, **13**, 2302647.
5 W. Zuo, J. Qiu, C. Hong, X. Liu, J. Li, G. F. Ortiz, Q. Li, S. Zheng, G. R. Zheng and Y. Yang, *ACS Appl. Energy Mater.*, 2019, **2**, 4914–4924.
6 S. Kumakura, Y. Tahara, K. Kubota, K. Chihara and S. Komaba, *Angew. Chem., Int. Ed.*, 2016, **55**, 12760–12763.
7 E. J. Kim, P. R. Kumar, Z. T. Gossage, K. Kubota, T. Hosaka, R. Tatara and S. Komaba, *Chem. Sci.*, 2022, **13**, 6121–6158.
8 K. Kubota and S. Komaba, *J. Electrochem. Soc.*, 2015, **162**, A2538–A2550.
9 P. Wang, Y. You, Y. Yin and Y. Guo, *Adv. Energy Mater.*, 2018, **8**, 1701912.
10 C. Delmas, J. Braconnier, C. Fouassier and P. Hagenmuller, *Solid State Ionics*, 1981, **3–4**, 165–169.
11 C. Zhao, Z. Yao, Q. Wang, H. Li, J. Wang, M. Liu, S. Ganapathy, Y. Lu, J. Cabana, B. Li, X. Bai, A. Aspuru-Guzik, M. Wagemaker, L. Chen and Y.-S. Hu, *J. Am. Chem. Soc.*, 2020, **142**, 5742–5750.
12 N. Yabuuchi, M. Kajiyama, J. Iwatate, H. Nishikawa, S. Hitomi, R. Okuyama, R. Usui, Y. Yamada and S. Komaba, *Nat. Mater.*, 2012, **11**, 512–517.
13 X. Gao, L. Fang, H. Wang, S. Lee, H. Liu, S. Zhang, J. Gao, Y. Mei, M. Park, J. Zhang, M. Chen, L. Zhou, W. Deng, G. Zou, H. Hou, Y. Kang and X. Ji, *Adv. Funct. Mater.*, 2023, **33**, 2212685.
14 Y. You, A. Dolocan, W. Li and A. Manthiram, *Nano Lett.*, 2019, **19**, 182–188.
15 V. Duffort, E. Talaie, R. Black and L. F. Nazar, *Chem. Mater.*, 2015, **27**, 2515–2524.
16 M. H. Han, N. Sharma, E. Gonzalo, J. C. Pramudita, H. E. A. Brand, J. M. López Del Amo and T. Rojo, *J. Mater. Chem. A*, 2016, **4**, 18963–18975.
17 W. Zuo, J. Qiu, X. Liu, F. Ren, H. Liu, H. He, C. Luo, J. Li, G. F. Ortiz, H. Duan, J. Liu, M.-S. Wang, Y. Li, R. Fu and Y. Yang, *Nat. Commun.*, 2020, **11**, 3544.
18 S. Jia, S. Kumakura and E. McCalla, *Energy Environ. Sci.*, 2024, **17**, 4343–4389.
19 S. Chu, X. Jia, J. Wang, K. Liao, W. Zhou, Y. Wang and Z. Shao, *Composites, Part B*, 2019, **173**, 106913.
20 J.-Y. Hwang, T.-Y. Yu and Y.-K. Sun, *J. Mater. Chem. A*, 2018, **6**, 16854–16862.
21 Y. Zhou, L. Li, Y. Wu and H. Xie, *Eur. J. Inorg. Chem.*, 2023, **26**, e202200685.
22 Y. Li, Z. Yang, S. Xu, L. Mu, L. Gu, Y. Hu, H. Li and L. Chen, *Advanced Science*, 2015, **2**, 1500031.
23 X. Li, J. Xu, H. Li, H. Zhu, S. Guo and H. Zhou, *Advanced Science*, 2022, **9**, 2105280.
24 Y. Chen, Q. Shi, S. Zhao, W. Feng, Y. Liu, X. Yang, Z. Wang and Y. Zhao, *Batteries*, 2023, **9**, 183.
25 T.-Y. Yu, J. Kim, J.-Y. Hwang, H. Kim, G. Han, H.-G. Jung and Y.-K. Sun, *J. Mater. Chem. A*, 2020, **8**, 13776–13786.
26 H. Tanaka, S. Matsumoto, S. Kuze and T. Yamaguchi, *82nd Annual Meeting of the Electrochemical Society of Japan*, Yokohama, 2015, p. 3J29.
27 L. Zhang, J. Deshmukh, H. Hijazi, Z. Ye, M. B. Johnson, A. George, J. R. Dahn and M. Metzger, *J. Electrochem. Soc.*, 2023, **170**, 070514.
28 L. Zheng, J. C. Bennett and M. N. Obrovac, *J. Electrochem. Soc.*, 2019, **166**, A2058–A2064.
29 Q. Tao, H. Ding, H. Zhao, J. Huang, B. Dai and J. Li, *J. Alloys Compd.*, 2024, **976**, 172977.
30 M. Matsuzaki, R. Tatara, K. Kubota, K. Kuroki, T. Hosaka, K. Umetsu, N. Okada and S. Komaba, *Batteries Supercaps*, 2024, **7**, e202400009.
31 E. Nishibori, M. Takata, K. Kato, M. Sakata, Y. Kubota, S. Aoyagi, Y. Kuroiwa, M. Yamakata and N. Ikeda, *Nucl. Instrum. Methods Phys. Res., Sect. A*, 2001, **467-468**, 1045–1048.
32 R. B. V. Dreele and B. H. Toby, *GSAS II Developers Documentation*, 2025, p. 93243d.
33 R. Berthelot, D. Carlier and C. Delmas, *Nat. Mater.*, 2011, **10**, 74–80.
34 N. Yabuuchi, R. Hara, K. Kubota, J. Paulsen, S. Kumakura and S. Komaba, *J. Mater. Chem. A*, 2014, **2**, 16851–16855.
35 A. Jain, S. P. Ong, G. Hautier, W. Chen, W. D. Richards, S. Dacek, S. Cholia, D. Gunter, D. Skinner, G. Ceder and K. A. Persson, *APL Mater.*, 2013, **1**, 011002.
36 L. Sun, Y. Xie, X. Liao, H. Wang, G. Tan, Z. Chen, Y. Ren, J. Gim, W. Tang, Y. He, K. Amine and Z. Ma, *Small*, 2018, **14**, 1704523.
37 M. Matsui, F. Mizukoshi, H. Hasegawa and N. Imanishi, *J. Power Sources*, 2021, **485**, 229346.
38 Z. Wang, R. Hu, H. Chen, Y. Ye, Q. Zhao, Z. Du and S. Yang, *Energy Environ. Sci.*, 2025, **18**, 6832–6840.
39 Z. Sun, M. Gong, J. Li, M. Dong, K. Fan, X. Chang, F. Li, P. Hou and X. Xu, *J. Phys. Chem. C*, 2025, **129**, 6594–6604.
40 S.-B. Wei, Y.-J. He, Y. Tang, H.-W. Fu, J. Zhou, S.-Q. Liang and X.-X. Cao, *Rare Met.*, 2024, **43**, 5701–5711.
41 Y. Yang, Z. Wang, C. Du, B. Wang, X. Li, S. Wu, X. Li, X. Zhang, X. Wang, Y. Niu, F. Ding, X. Rong, Y. Lu, N. Zhang, J. Xu, R. Xiao, Q. Zhang, X. Wang, W. Yin, J. Zhao, L. Chen, J. Huang and Y.-S. Hu, *Science*, 2024, **385**, 744–752.
42 G. Brugnetti, C. Triolo, A. Massaro, I. Ostroman, N. Pianta, C. Ferrara, D. Sheptyakov, A. B. Muñoz-García, M. Pavone, S. Santangelo and R. Ruffo, *Chem. Mater.*, 2023, **35**, 8440–8454.
43 Ş. Patat, A. Şahin, Y. Taş, F. Şanlı, Y. Yılmaz and T. Öztürk, *Int. J. Energy Res.*, 2022, **46**, 22025–22037.
44 H. Kim, C.-E. Yang, S. Lee, B. Yun, T. Kim, S. Lee, J. H. Chang, B. T. Na, H. Lee, Y. Kim and K. T. Lee, *ACS Mater. Lett.*, 2025, **7**, 1003–1011.
45 C. Lee, M. Shimizu, R. Tatara, K. Nakamoto, T. Hosaka, Z. T. Gossage and S. Komaba, *ACS Appl. Energy Mater.*, 2025, **8**, 5867–5877.
46 Y. Yoda, K. Kubota, H. Isozumi, T. Horiba and S. Komaba, *ACS Appl. Mater. Interfaces*, 2018, **10**, 10986–10997.
47 Y. Liu, K. Han, D. Peng, L. Kong, Y. Su, H. Li, H. Hu, J. Li, H. Wang, Z. Fu, Q. Ma, Y. Zhu, R. Tang, S. Chou, Y. Xiao and X. Wu, *InfoMat*, 2023, **5**, e12422.
48 D. Bresser, D. Buchholz, A. Moretti, A. Varzi and S. Passerini, *Energy Environ. Sci.*, 2018, **11**, 3096–3127.